Particle Seeding System Upgrades in the NASA GRC 1'×1' Supersonic Wind Tunnel

Heath H. Reising* and Puja Upadhyay [†]
HX5 LLC, Brook Park, OH, 44142

Mark P. Wernet[‡]
NASA Glenn Research Center, Cleveland, OH, 44135

An effort to improve the particle-based velocity measurement capability in the NASA Glenn Research Center 1'×1' Supersonic Wind Tunnel has recently been undertaken. Modifications to the pressure vessel where the seed particles are generated and inserted into the wind tunnel's pressurized air supply were implemented to reduce residence time and thus agglomeration of particles in the seeding tank. The operation of the improved seeding system was evaluated and optimized using particle image velocimetry (PIV) measurements across an isolated oblique shock wave in the facility test section. The PIV system using optimal seeding settings was also applied to make detailed measurements of the test section sidewall boundary layer height to inform model designs for future testing in this facility.

Nomenclature

C_D = drag coefficient
d = diameter
Kn = Knudsen number
l = distance
Ma_p = particle slip Mach number
Re = Reynolds number
t = time
u = streamwise velocity
$\vec{U}$ = velocity vector
x = streamwwise coordinate, $x = 0$ at leading edge of test section
y = wall-normal (spanwise horizontal) coordinate
δ_{99} = boundary layer thickness, y ($U = 0.99U_\infty$)
θ = local flow angle in x-y plane
ξ_P = particle relaxation distance
τ_P = particle relaxation time

Superscripts/Accents

$*$ = non-dimensionalized across shock wave
$\widehat{}$ = estimated

Subscripts

1 = upstream of shock wave
2 = downstream of shock wave
f = fluid
n = shock-normal
p = particle

---

*Research Engineer, Inlets and Nozzles Branch, 21000 Brookpark Rd M/S 5-12, AIAA Senior Member.
[†]Research Engineer, Inlets and Nozzles Branch, 21000 Brookpark Rd M/S 5-12, AIAA Member.
[‡]Research Engineer, Optics and Photonics Branch, 21000 Brookpark Rd M/S 77-1, AIAA Associate Fellow.

pg = particle generator
tp = tank purge

I. Introduction

Particle image velocimetry (PIV) is a measurement tool used frequently at the NASA Glenn Research Center (GRC). The technique has been applied in large-scale wind tunnel facilities, such as the 10'×10'[1] and 9'×15'[2] Wind Tunnels, as well as extensively used in the jet facilities of the Aero-Acoustic Propulsion Laboratory[3–5] and turbomachinery facilities of the Engine Research Building[6]. The 1'×1' Supersonic Wind Tunnel has historically served as a venue for prototype testing at reduced scale and cost relative to the 10'×10', but is notably lacking in published or varied applications of the PIV measurement technique.

Laser Doppler anemometry measurements have been previously applied in this facility using a particle seeding configuration which has since evolved into the one used in this test[7]. In the intervening years since, the particle image velocimetry technique has been applied to expedite the collection of velocity data. In these tests, the observed velocity fields exhibited a smoothing effect in regions of high velocity gradient which is typical of particle-based velocimetry measurements where seed particle inertia becomes non-negligible relative to the particle drag. Estimates of the droplet diameter within the test section ranged up to 4 μm. The suspected cause of the large seed particles was agglomeration within the pressure vessel where they are generated. The current campaign was initiated to reduce the seed particle size by making modifications to the particle injection system to reduce the particle residence time in the seeding chamber, thus improving the PIV measurement accuracy in regions of high velocity gradient.

II. Apparatus and Procedure

A. Test Facility

The NASA GRC 1'×1' Supersonic Wind Tunnel is a continuous flow facility capable of providing test section Mach numbers ranging from 1.3 to 6[8]. The interchangeable 2D converging-diverging nozzles can be rapidly exchanged using the hydraulic jack system, making this facility a versatile tool for small-scale aerodynamic testing. The test section is configurable with various window and wall inserts to fit the needs of the current test. In this test, the test section was configured to be 12.2 inches wide, 12 inches high, and 53 inches long.

The ability of the facility to operate continuously is made possible by the use of lab-wide shared compressed air and vacuum sources. The compressed air (commonly called "combustion air" at GRC) source can provide clean, dry air at either 40 psig or 150 psig. Vacuum is typically provided at 26" Hg. These pressures allow for operation over a wide range of Mach numbers; the current test utilizes only the Mach 2.5 and Mach 3.5 nozzle blocks.

The current test focuses on improving the performance of the facility's particle seeding tank, which is used when PIV measurements are required. The approximate location of the tank within the 1'×1' Wind Tunnel complex is shown in Figure 1 below. The outlet of the tank is connected to the facility's combustion air supply piping just aft of the filtering elements to avoid clogging them with seed material.
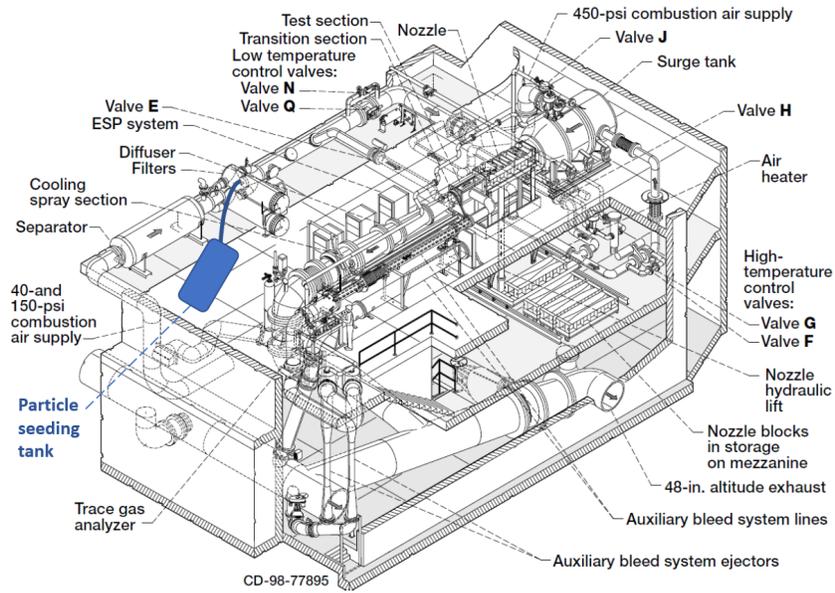
Fig. 1   Diagram of the 1'×1' Supersonic Wind Tunnel facility highlighting the location of the particle seeding tank in the basement[8].

B. Test Chronology

PIV data were collected during this test for two distinct purposes: seed particle size quantification and sidewall boundary layer height assessment. The particle sizing measurements were made to evaluate the effectiveness of changes made to the seeding tank and to optimize its operation. Additional measurements were made along the wind tunnel test section sidewall which required only a minor shift of the camera field of view. This data was intended to quantify the boundary layer height to inform the design of an inlet model scheduled for future testing.

For the particle sizing tests, a simple half-diamond wedge model was fabricated and installed to generate a shock wave of known strength in the test section. This shock wave provides an impulsive perturbation to the direction and velocity of the air flow which can be used to assess how faithfully the seed particles track the deceleration of the gas across the shock. Further detail on how this flowfield is used to quantify the particle size will be given in Section III.A. A photograph of the 18° wedge installed in the wind tunnel test section is shown in Figure 2. The wedge was offset from the tunnel sidewall by 2 inches on a pair of struts and had a span of 10 inches.

Fig. 2   18° wedge model installed in the 1'×1' Wind Tunnel test section (forward looking aft).

3

For the seeding optimization, the wind tunnel was operated with the maximum total pressure available using the lab-wide 40 psig combustion air supply. The flow rate of purge air through the seeding tank was varied by changing the set point on a pressure regulator. The pressure of N_2 supplied to the smoke generators has a strong effect on the particle quantity and size, and thus was varied during testing to identify a set point which provided optimal seeding within the test section. After processing the results from the seed particle optimization tests, the optimal pressure settings for the tank purge and N_2 supply to the smoke generators were used for all subsequent testing.

An additional objective of this test campaign was to assess the test section sidewall boundary layer height at the most forward station possible. This requirement drove the decision to move the laser ingress window forward within the test section. Ultimately, the schlieren window used to observe the particle scattering limited the measurement region to 134 mm downstream of the test section leading edge.

C. Particle Image Velocimetry Measurement System

1. Seeding Tank

The seeding tank is comprised of a 37" long 30" nominal pipe size (NPS) cylindrical body with Class 150 flanges on either end. This tank houses a pair of ViCount 5000 particle generator devices which generate oil droplets which are nominally 0.3 µm in diameter. Installing the particle generators within the pressure vessel allows for them to be connected to the pressurized combustion air upstream of the wind tunnel without over-pressurization. The N_2 gas supply to these particle generators as well as all of the electrical connections enter the tank through various couplings welded around the circumference of the tank. In the past, shop air was supplied to the tank through 1/2" diameter tubing (purge line) to generate a prevailing flow through the tank and prevent stagnation. A section view of the legacy configuration of the tank is presented in Figure 3. The small size of the purge air supply line was suspected to be the root cause of large seed particles due to the inadequate purging flow leading to long particle residence times in the tank and, ultimately, particle agglomeration.
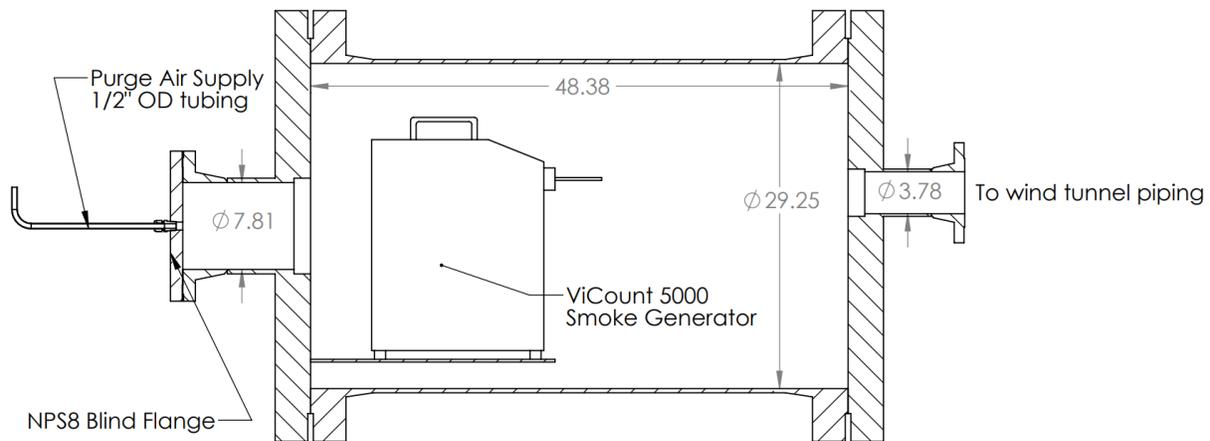
Fig. 3 Elevation section view of legacy PIV particle seeding tank configuration. *Particle generator arrangement and tank are symmetric about the section plane.*

A simple upgrade to this configuration was conceived which would require only an increase in the size of the air supply piping. However, it was unknown whether simply adding more airflow would sufficiently purge the seed material from the tank. The tank internal flowfield with the proposed change was investigated with a simple CFD simulation performed using Solidworks® Flow Simulation. This package solves the RANS equations with a modified $\kappa - \epsilon$ turbulence model[9]. Figure 4 shows the result of this simulation, which assumed the included 2" NPS supply line supplied 1 lbm/s of purge air. As postulated, the purge flow passes directly through the center of the tank without driving the seeded air out of the tank. Seed particles are only picked up by entrainment in the periphery of the high-speed jet in the center of the tank, which would leave a significant amount to recirculate in the tank.

In order to more thoroughly purge and mix the seeded gas from the seeding tank, a distribution manifold was designed to be installed inside the seeding tank. This device, nicknamed the "wagon wheel," consisted of 8 radial pipes
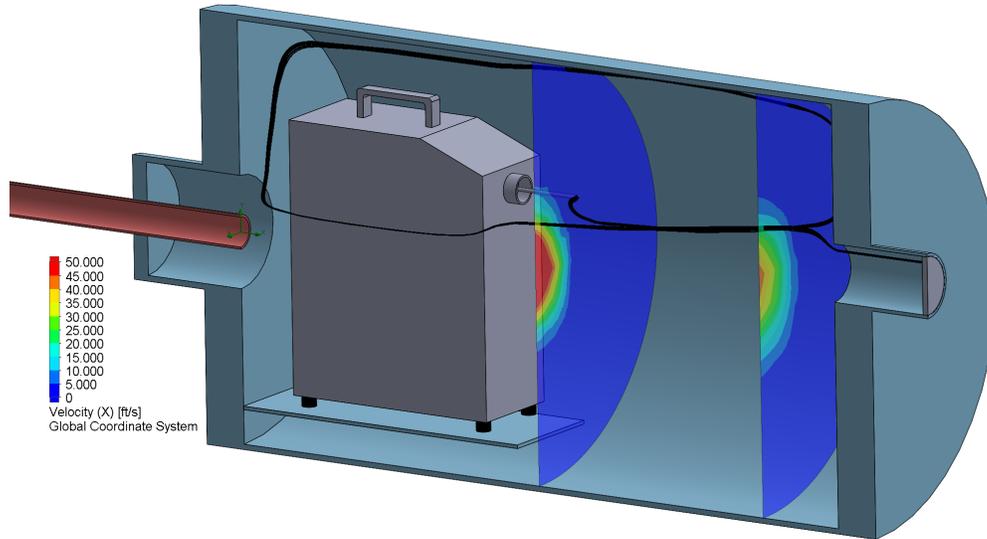
Fig. 4 CFD solution for legacy PIV particle seeding tank configuration with increased purge air capability. *Particle generator arrangement and tank are symmetric about the section plane.*

with an axial distribution of holes on each "spoke." The device and its location when installed within the seeding tank is shown in Figure 5 below. The optimal layout of hole spacing and diameters on each spoke was determined through a parametric CFD study using Solidworks® Flow Simulation. A sample solution at the operating point at the maximum capacity of the shop air system (2 lbm/s) is shown by the contours and particle traces in Figure 5. Due to the improved distribution of supplied air around the periphery of the tank, particle-laden flow exiting the smoke generators is rapidly drawn toward the tank axis and to the outlet piping which significantly reduces the particle residence time in the tank.
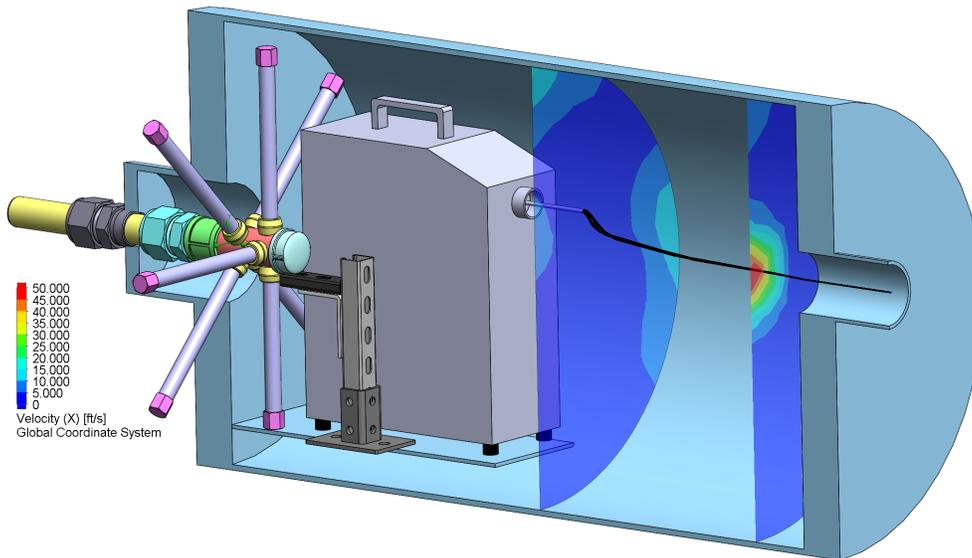
Fig. 5 Upgraded PIV particle seeding tank configuration operating at 2 lbm/s of buffer flow. *Particle generator arrangement and tank are symmetric about the section plane.*

2. Optical Components

For this test, the laser was located on the port (East) side of the wind tunnel and the beam entered the test section through the sidewall in that direction. The lasers (Continuum Surelite III) provided around 380 mJ per pulse from each cavity at 532 nm. A periscope assembly was used to bring the laser beam up to the height of the test section centerline. This was attached directly to the cart containing the laser head. In the upward leg of the periscope, the nominally 10 mm circular beam was formed into a sheet using -30 mm and -25 mm cylindrical lenses. The sheet was focused to approximately 1 mm thick using a 2 m spherical lens. This system resulted in a sheet which covered approximately 20 cm in the streamwise direction in the test section and the region of interest.

The laser, sheet forming optics, and periscope were placed inside enclosures to contain stray light. The camera (Princeton Instruments ES4020) was mounted off an overhead beam above the test section in order to view the region of interest from one of the facility's standard schlieren windows. The locations of the PIV system components relative to the test section are depicted in Figure 6a.

The camera fields of view for both phases of the test are shown in Figure 6b below. These were obtained using an 85mm focal length lens on the camera. The camera was outfitted with a mechanical shutter to prevent overexposure due to the mismatch in operating frequencies between the laser and cameras (2 Hz and 10 Hz, respectively)[1]. The interior of the test section and the wedge model were painted black in order to minimize laser reflections in the background of the particle images. Additionally, the camera sensor was precisely shielded from laser flare from impingement on the sidewall or wedge with sheet metal pieces and electrical tape placed above the test section window.

(a) Component locations relative to wind tunnel test section.

(b) Measurement regions for each phase (plan view).
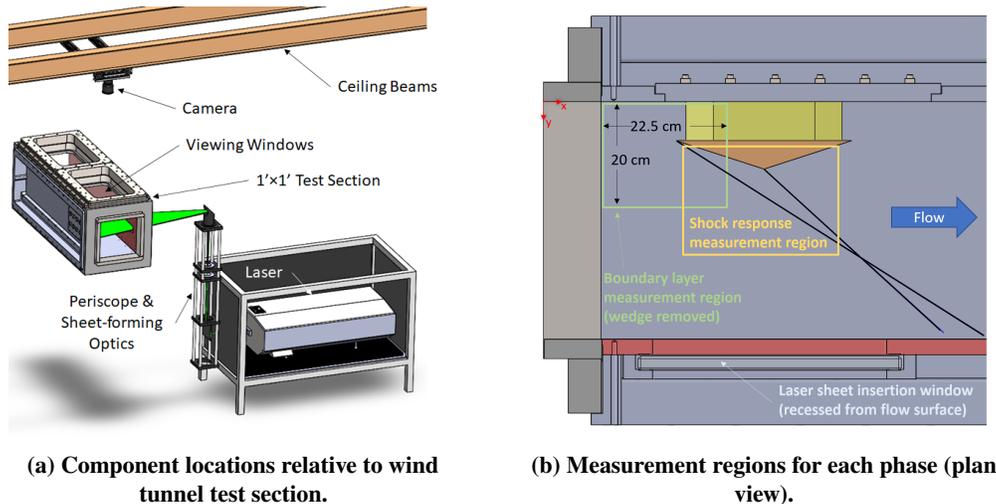
Fig. 6   PIV system arrangement.

An existing glass window and retainer frame assembly was reused for this test to reduce cost. A standard test section sidewall was modified to place the window more forward in the test section than its previous application. One downside of this window design is the recessed cavity generated by the window, which is shown in Figure 6b. While this cavity was not expected to disturb the region of interest aerodynamically, some amount of seed material accumulation was expected on the window which will be discussed in Section III.B.

III. Results and Discussion

A. Particle Size Assessment

Particle lag effects due to the finite inertia of the tracer particles are commonly quantified *in situ* in supersonic flows by observing the particle response lag through a shock wave[10–12]. Typically, the resulting measurements of particle relaxation time of polydisperse particle clouds by this method can be biased toward larger particles due to their higher scattering intensity[13]. This is an unavoidable artifact of the PIV cross-correlation method which requires multiple particles per interrogation window. With no superior alternative method available, this shock response method was utilized to assess the particle response in the 1'×1' Wind Tunnel.

As described in Section II.B, a planar shock generator plate was installed in the wind tunnel test section to quantify the size of the PIV seed particles based on their response to the sharp velocity gradient across the resulting oblique shock. With the shock generator plate set at 18°, sets of 400 PIV image pairs were collected for discrete combinations of tank purge (P_{tp}) and seeder N_2 pressure (P_{pg}) spanned by the values given in Table 1. The delay times between PIV image pairs, Δt, were selected such that the maximum particle displacements in each case was approximately 8 pixels.

Table 1   Test conditions – seeder optimization.

M_0	P_{t0} [psia]	T_{t0} [°R]	P_{pg} [psig]	P_{tp} [psig]	Δt [µs]
2.47	50	517 ± 2	65–105	50–70	2.5
3.46	55	531 ± 2	55–85	55–70	1.8

While the 1'×1' is capable of continuous operation, the duration of these PIV tests was limited to approximately 30 seconds after the particle generators were activated. This is due to oil build-up on the test section walls occluding the viewing windows. There is also likely an effect on the sheet focus quality as oil builds up on the window through which the beam enters the test section. This is an unavoidable consequence of the global seeding technique and the long propagation distance between the seeding tank and the tunnel test section. In other facilities at GRC, a local seeding technique has been applied to only seed the regions of the flow where measurements are desired[14]. However, due to the complexity of this facility, this method is not easily implemented. Thus, PIV testing in this test facility requires manual cleaning between recording each PIV dataset. Future PIV installations may utilize a purge air-stream over the laser sheet window and PIV camera window to keep these surfaces cleaner for a longer duration.

Each PIV dataset was processed with varying final pass subregion size, as will be discussed. Shock-normal velocity profiles were extracted along the length of the shock and normalized in the typical fashion to produce response profiles such as the example shown in Figure 7b. If particle drag is assumed to be a linear function of the slip velocity, then particle velocity in response to an impulsive change in fluid velocity should decay exponentially in space as

$$\ln(u_n^*) = \ln\left(\frac{u_n - u_{2n}}{u_{1n} - u_{2n}}\right) = -\frac{t}{\tau_p} \cong -\frac{l_n}{\xi_p}. \tag{1}$$

Here, the relaxation in spatial coordinate, l_n, is converted to relaxation in time units by assuming a linear relationship between $\frac{t}{\tau_p}$ and $\frac{l_n}{\xi_p}$ [12]. Using the guidelines given in Ref. 12, the particle response times were evaluated by a linear fit of data in the $-2 \le \ln(u_n^*) \le -0.5$ range. The fit for this particular case yields a relaxation time of 1.8 µs. The vector pitch resulting from the selected combination of interrogation window size and overlap resulted in three points being located within the fitted velocity range. However, this is dependent on the sharpness of the velocity decay profile; more sharp profiles may only contain 2 points for fitting. The small bounce in the velocity profile downstream of the initial velocity drop is attributable to very weak waves in the test section (logarithmic scaling emphasizes this velocity jump; it is $O(1$–$2\,\frac{m}{s})$.

Detailed analysis was performed to determine not only the mean particle size behavior, as shown in Figure 7, but also in a statistical sense. Particle response times were evaluated across shock interface row-by-row within each velocity snapshot and then compiled across an entire dataset. This allows for the evaluation of not only the average behavior, but also the distribution of particle sizes within the dataset. This technique should highlight the broadness of the particle size distribution and also any multimodality due to stray particles from other sources in the facility piping.

To investigate the effect of PIV data density on the particle response time results, the velocity profile fitting procedure was also applied to vector fields computed with increased interrogation region overlap and reduced interrogation region size. Figure 8 shows probability density distributions for derived particle lag times and their respective median values. It is clear that halving the final interrogation window size has a dramatic effect on the resulting median particle response time. Adding more data points by increasing window overlap further reduces the particle response times and also creates a tighter distribution.

The effect of PIV interrogation region size was analyzed with synthetic PIV data in Ref. 12 and found to require PIV window sizes of the same order as ξ_p or smaller. In the current test, a typical ξ_p value is 0.5–2 mm; thus, with an image scale of 0.107 $\frac{mm}{pix}$, a 16×16 window with 75% overlap just meets this criteria. In practice, increasing the overlap to 87.5% was found necessary to guarantee at least 2 data points within the analyzed velocity range of $-2 \le \ln(u_n^*) \le -0.5$. With the addition of (essentially interpolated) data within the velocity decay profiles, spurious results from edge cases where the vector spacing places a point just outside those limits are rectified.

(a) Mean velocity field flow angle in x-y plane, θ.

(b) Sample particle response profile and fit.
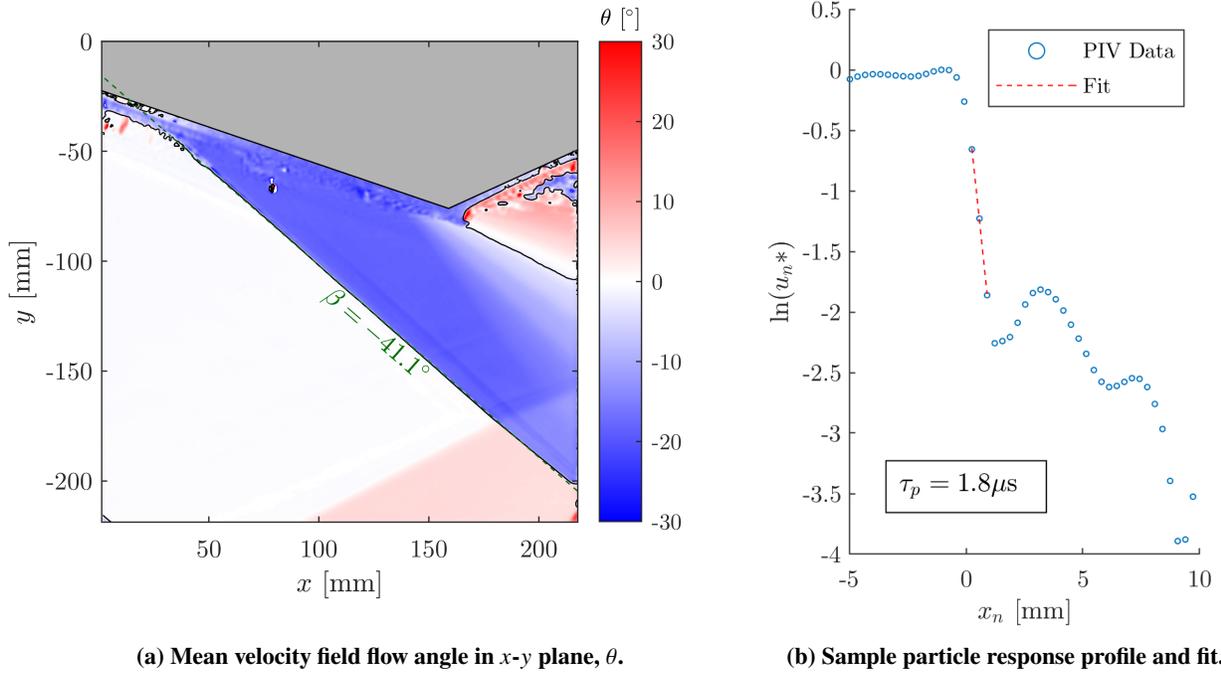
Fig. 7 Shock response velocity field at $M_0 = 2.5$ and $P_{pg} = 65$ psig using 16×16 windows and 87.5% overlap.

In this case, the shortest median relaxation time is observed with 16×16 regions and maximum overlap. Further reduction in window size produces distributions with similar peak values, but a much broader spread. This is attributed to noise in the vectors due the reduction in signal-to-noise of the correlation peak from insufficient particles appearing in the interrogation windows. Both 8×8 windows at 75% overlap and 4×4 windows at 50% overlap have the same vector grid spacing as the optimal case; thus, differences driven by vector field resolution should be minimal. Instead, the broadening seen in the distributions for the smallest windows is ascribed to scarce seed material at those fine scales. This illustrates an important trade-off when using shock response measurements to size PIV particles: high camera magnification must be selected to adequately resolve the post-shock velocity decay, but adequate seeding density for the required scale is usually unavailable or creates other issues such as occlusion of the viewing windows. The secondary peak at $\tau_p \approx 2.5\,\mu$s is physically relevant and will discussed later in terms of the particle physical size.

As an aside, the surprising result of obtaining valid vectors at 8 pixel and smaller interrogation windows should be addressed. These small window sizes work in this flowfield only due to the relatively low velocity dynamic range required (essentially two uniform regions pre- and post-shock). Additionally, the interrogation windows are not truly square and binary, but instead use the Gaussian window weighting capability of the PIV processing software (LaVision® DaVis 10) which uses a pixel region somewhat larger than the nominal dimensions. In the absence of an arbitrary user-defined data quality metric on correlation or peak ratio value, small interrogation windows yield results which are remarkably accurate in the mean. However, the correlation peak noise due to a lack of particles within the window produces the aforementioned scatter in the velocity data, which is apparent in the individual velocity field realizations which are analyzed here.

Although particle response time is adequate to describe the aerodynamic response of the seed particles, the computed lag times were converted to particle diameter in order to quantify their physical size relative to the specifications given by the manufacturer of the particle generator. The standard differential equation for a droplet of constant size traveling in a gas is

$$\frac{d\overrightarrow{U_P}}{dt} = -\frac{3}{4}C_D Re_p \frac{\mu}{\rho_p d_p^2}(\overrightarrow{U_P} - \overrightarrow{U_f}). \tag{2}$$

Typically when applying Equation 2, the Stokes drag relation $C_D = \frac{24}{Re_p}$ is used. However, in the compressible regime, both rarefaction and fluid inertia effects can alter the particle drag by over an order of magnitude from the typical Stokes

8
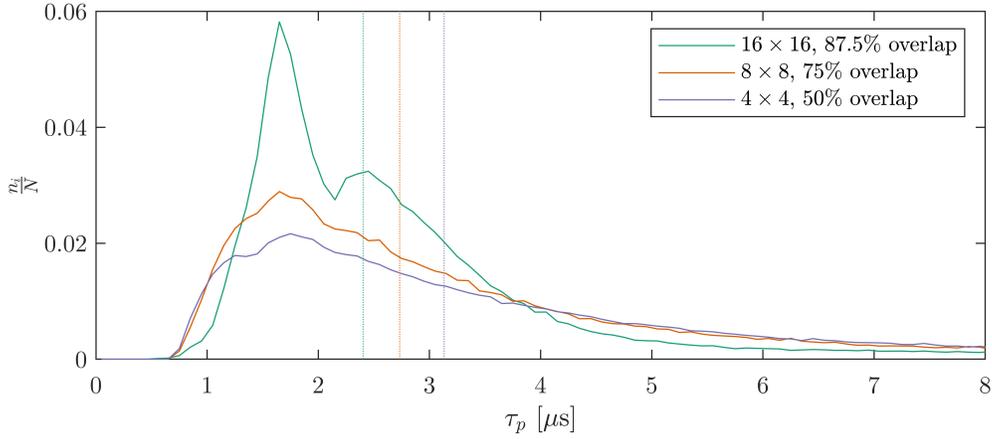
Fig. 8 Particle relaxation time probability density distributions with varying PIV interrogation window parameters. *Same dataset as Figure 7. Dashed lines show median value for each distribution.*

drag model[15, 16]. Figure 9 shows the operating conditions for this particular test setup overlaid on a contour plot of the particle drag normalized by the Stokes drag value. At worst case, the true particle drag will be reduced to 46% of the Stokes drag value due to non-continuum effects. This occurs for the smallest particles (0.3 µm) at the high Mach number condition, where the Knudsen number is 0.43. At the other bounding conditions, the drag coefficient is very near or higher than the Stokes model value.
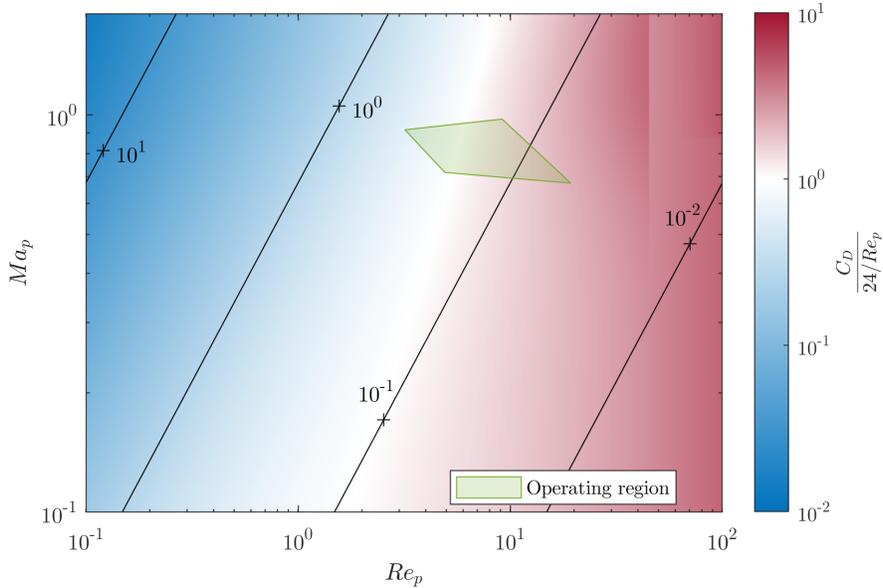
Fig. 9 Variation in particle drag relative to Stokes' model[15] showing operating boundaries of the current test. *Lines of constant Kn are shown in black and labeled. Test conditions from Table 1 and a particle size range of 0.3–1.0 µm were used to generate operating region bounds.*

Figure 10 shows particle size histograms for a range of P_{pg} for a test section freestream Mach number of 2.5. The pressure of the air supplied to purge the tank was operated at the maximum condition that the building shop air could sustain (70 psig) for all the results shown. As the pressure of the N_2 supplied to the smoke generator (P_{pg}) increases, there is an increase in larger particles in the tail of the particle size distribution and, thus, the median particle size increases. At the optimal input pressure of $P_{pg} = 65$ psig, the particle size histogram shows the same character as

that in Figure 8 with the primary peak at approximately 1.7 μs moving to the 0.55–0.6 μm bin. The secondary peak is centered almost exactly $\sqrt[3]{2}$ larger, which is the expected diameter for a combined droplet from the collision of two droplets of the most common size.

(a) P_{pg} = 65 psig.

(b) P_{pg} = 75 psig.

(c) P_{pg} = 85 psi.

(d) P_{pg} = 105 psi.
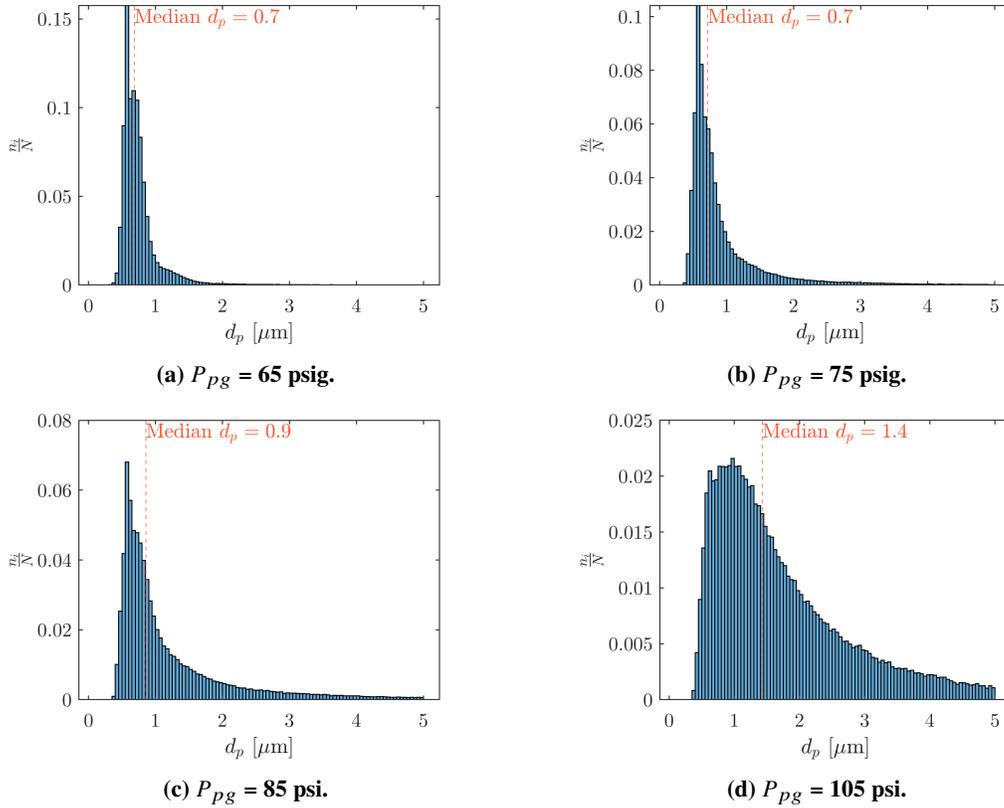
Fig. 10   Computed particle diameter histograms at $M_0 = 2.5$ and $P_{tp} = 70$ psig using PIV vectors computed with 16×16 windows at 87.5% overlap.

As the testing proceeded to a higher Mach number (lower facility mass flow rate), the lower limit on P_{pg} for which particles would still be produced by the smoke generator was further explored. Again, the most favorable seed particle sizes were generated when the N_2 supply pressure was set to a minimal value. Figure 11 shows the particle size distribution at the optimal operating condition of P_{pg} = 65 psig.
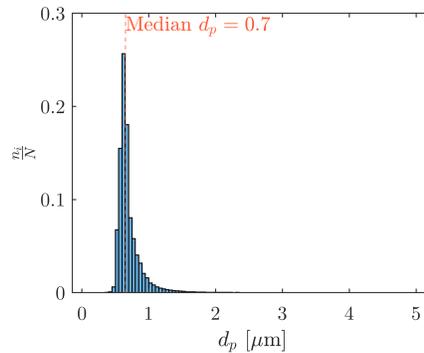
Fig. 11   Computed particle diameter histogram at optimal operating condition ($P_{pg} = 65$ psig, $P_{tp} = 70$ psig) for $M_0 = 3.5$ using PIV vectors computed with 16×16 windows at 87.5% overlap.

B. Sidewall Boundary Layer Characterization

After the improved seeding system had been characterized and optimal operating conditions had been identified, the shock generator wedge was removed from the test section sidewall leaving a "clean" test section. In this configuration, the camera field of view was moved toward the starboard sidewall to capture the naturally-occurring test section boundary layer. The same two facility nozzles were utilized since both are relevant to the follow-on test entry which requires the boundary layer height information. When the Mach 2.5 nozzle was installed, PIV datasets were collected at 4 discrete total pressure settings to additionally investigate the sensitivity of boundary layer height to Reynolds number. The same Δt values presented in Table 1 were utilized in this part of the test since freestream velocity at each M_0 is unchanged. The final pass interrogation regions used in processing these datasets was 32×32 pixels with 50% overlap.

Due to the strong reflection from the laser sheet impinging on the steel sidewall, several millimeters of the flowfield nearest to the wall were masked by a piece of sheet metal to protect the camera sensor from oversaturation. Thus, the current PIV measurement setup could complete the objective of quantifying the boundary layer height, but would not be able to generate detailed boundary layer profiles or provide integral parameters. As in the shock response testing, the test duration was limited by the rapid occlusion of the viewing window by oil attached to the test section surface. Only the first 120-150 images were useful for obtaining valid PIV data near the wall due to oil accumulation in the test section corner. This is evident from the sample images of Figure 12 where degradation of the image quality is apparent in the upper left portion of Figure 12b as streaks of oil attached to the test section walls progress into the field of view.

(a) Early in data record (just after seeding initiated).   **(b) After ~ 90 s of seeder operation.**
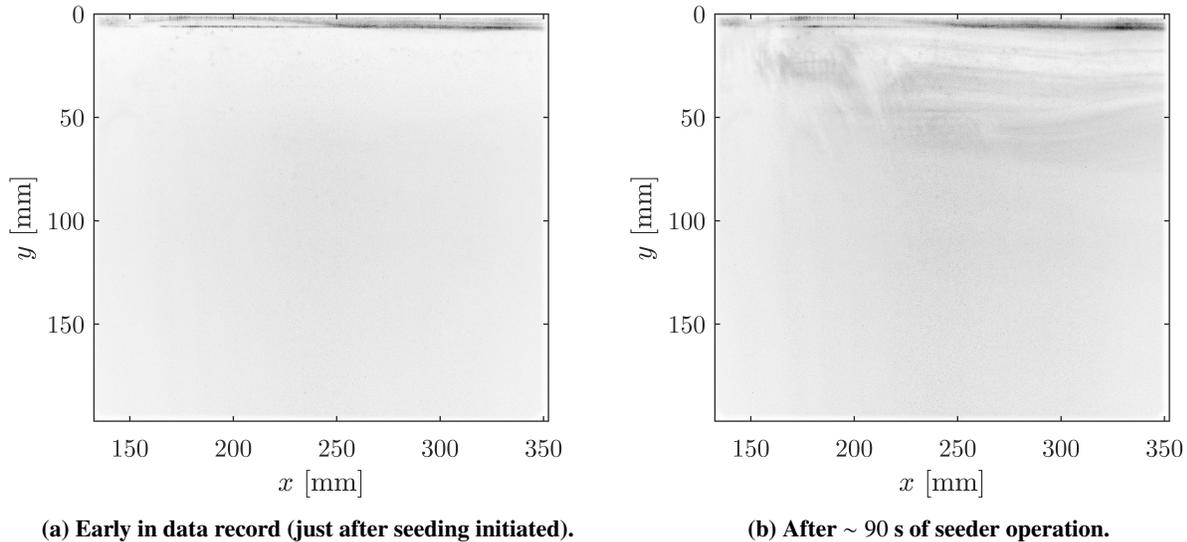
Fig. 12   Sample particle images during $M_0 = 3.5$ recording.

Figure 13 shows an ensemble mean velocity field at $M_0 = 2.5$ and maximum Reynolds number. Here, the typical characteristics of the velocity datasets are illustrated: data very near the wall is unavailable, but the outer portion of the boundary layer is clearly identifiable. The freestream velocity appears to be very uniform and is aligned with the horizontal axis of the camera sensor. The region of data used for computing the average boundary layer profile is bracketed by the vertical dashed lines in the figure. Data upstream of this region is polluted by spurious vectors which result from oil appearing on the viewing window. A balance must be struck between the number of velocity field instances used in the average and the usable region of velocity data on the upstream side as the oil streaks slowly progress aftward with each successive image pair.

Extracted wall-normal velocity profiles within the boundary layer are presented in Figure 14 for a selected streamwise position in the middle of the PIV field of view. Within each profile, velocity data is typically available for $U \geq 0.8U_\infty$, which is more than adequate to identify the location of δ_{99}. Here again, the uniformity of the mean freestream velocity is evident. Table 2 summarizes the results over all tested cases in this portion of the test entry. The expected behavior is observed; increases in test section Reynolds number yield a nearly linear reduction in the boundary layer height. These δ_{99} values agree well with a recent test where detailed Pitot rake measurements were made at $x = 133.4\,\text{mm}$, differing by less than 3% at Mach 2.5 and $P_{t0} = 50$ psia[17].
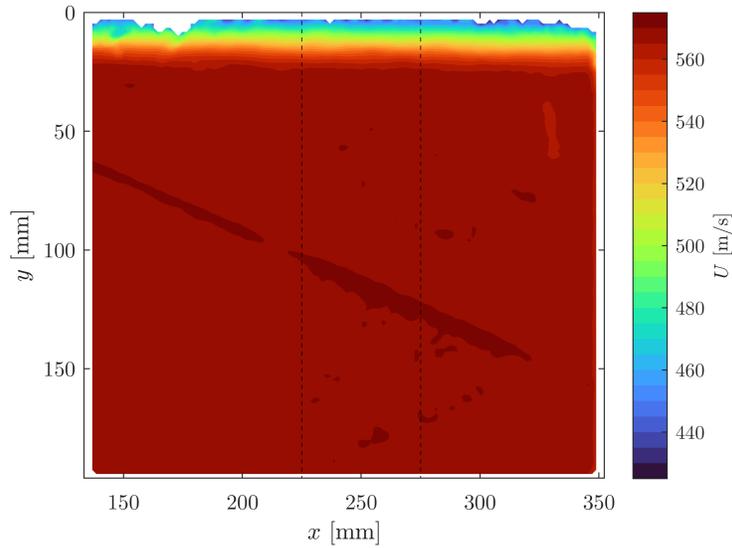
Fig. 13   Sidewall boundary layer mean flowfield at $M_0 = 2.5$ **maximum Reynolds number condition.**

Due to the limited scale of this facility's test section, the quantity of most interest to future test installations is the boundary layer height at (and upstream of) the leading edge of the test section ($x \leq 0$). This region is not easily probed by optical or conventional means. However, assuming an $x^{4/5}$ growth rate for a turbulent boundary layer with zero pressure gradient, extrapolations can be made using PIV-derived boundary layer heights at several axial stations within the region measured. The extrapolated boundary layer heights are presented as the last columns in Table 2 for the test section leading edge station. Although especially large models can be installed forward of this station, extrapolation further upstream from test section boundary layer data is not feasible as the nozzle sidewalls reflex outward into a 0.36° straight tapered section which blends the converging-diverging contour to the test section width.

(a) $M_0 = 3.5$ **and** $P_{t0} = 55$ **psia.**

(b) $M_0 = 2.5$ **and** $P_{t0} = 50$ **psia.**

(c) $M_0 = 2.5$ **and** $P_{t0} = 20$ **psia.**
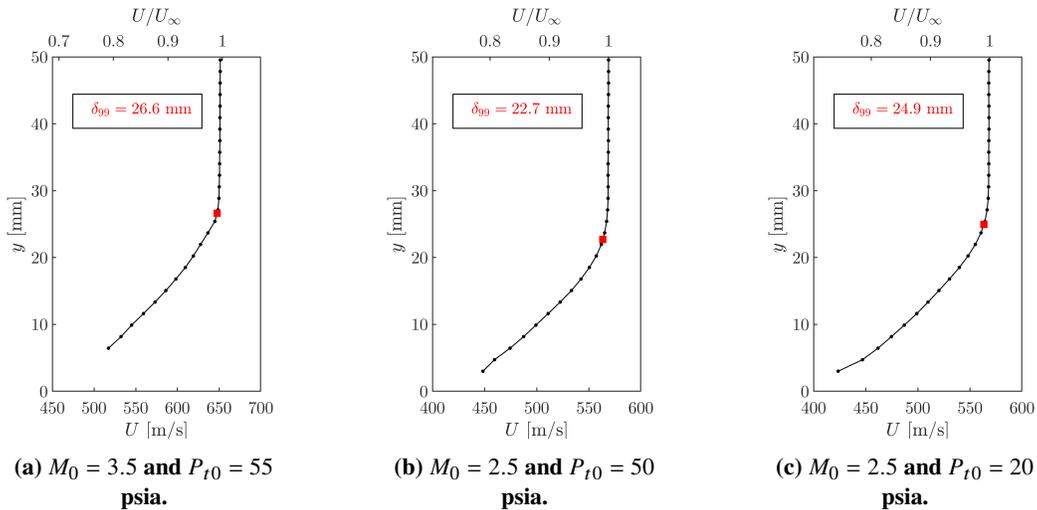
Fig. 14   Sidewall boundary layer velocity profiles at $x = 25$ **cm.**

The PIV data also provide an abundance of information about the freestream uniformity and turbulence level. Figure 13 shows the presence of a weak wave which traces almost exactly to the interface between the nozzle and test section which indicates a slight misalignment or small vacuum leak. Other than this insignificant artifact, the freestream

Table 2   Sidewall boundary layer height measurement summary.

M_0	P_{t0} [psia]	T_{t0} [°R]	P_{pg} [psig]	Re [ft^{-1}]	$\delta_{99}(x = 25$ cm) [mm]	$\widehat{\delta_{99}}(x = 0)$ [mm]
2.47	20	535 ± 2	65	4.45×10^6	24.9	19.1
2.47	30	535 ± 2	65	6.46×10^6	23.9	19.0
2.47	40	535 ± 2	65	8.45×10^6	23.1	18.7
2.47	50	535 ± 2	65	10.7×10^6	22.7	18.1
3.46	55	535 ± 2	65	6.99×10^6	26.6	24.7

flow appears to be wave-free and very uniform. This is confirmed quantitatively in the mean velocity histograms of Figure 15. Overall, the spatial variation in mean velocity is less than ±1% for both cases. The bimodality seen in both distributions is the manifestation of the velocity change across the weak wave which traverses the measurement region. This velocity change is slightly more pronounced at higher Mach number, as expected. The ability of the PIV measurement to detect this weak wave illustrates the quality of the freestream velocity data.

The distribution of turbulent fluctuations from the local time-average velocity are shown in Figure 16. Both streamwise and wall-normal fluctuations behave as normal distributions. The measured root-mean-square intensities for u' are 0.42 and 0.41 % at Mach 2.5 and Mach 3.5, respectively. These turbulence levels are within the typical range for a supersonic wind tunnel of this type where no attempt is made to reduce the turbulence generated by the nozzle boundary layers[18].

(a) $M_0 = 2.5$ and $P_{t0} = 50$ **psia.**

(b) $M_0 = 3.5$ and $P_{t0} = 55$ **psia.**
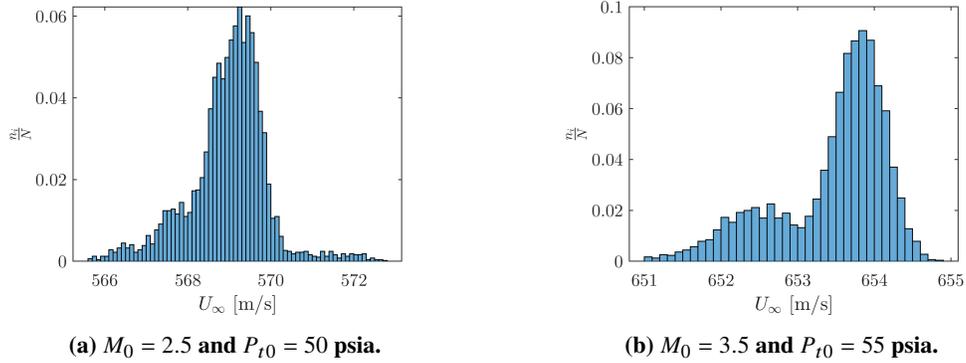
Fig. 15   Freestream ($y > 2\delta_{99}$) time-average velocity distributions.

(a) $M_0 = 2.5$ and $P_{t0} = 50$ **psia.**

(b) $M_0 = 3.5$ and $P_{t0} = 55$ **psia.**
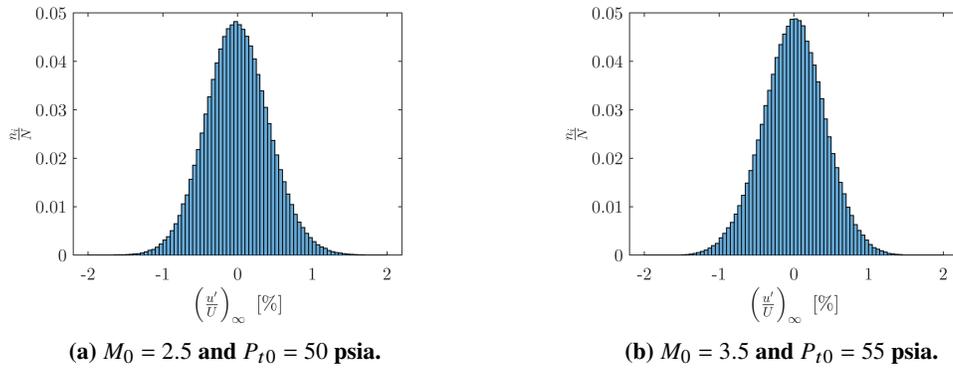
Fig. 16   Freestream ($y > 2\delta_{99}$) velocity fluctuation distributions.

IV. Conclusions

The oil droplet seeding system in the NASA GRC 1'×1' Supersonic Wind Tunnel has been upgraded to reduce the median particle size. This improves the accuracy of the particle image velocimetry measurement technique by reducing the inertia of the seed particles. A reduction of over 5× in median particle diameter was realized by the installation of a new purge flow distribution manifold. The performance of the revised system was evaluated and optimized through analysis of PIV measurements made across an oblique shock wave. Under optimal operating conditions, the median particle size was shown to be $0.7\,\mu m$ across large variation in wind tunnel mass flow. Additional PIV data was obtained near the test section sidewall to characterize the boundary layer extent and freestream turbulence levels to inform future test installations.

Acknowledgments

References

[1] Wernet, M., Locke, R., Wroblewski, A., and Sengupta, A., "Application of Stereo PIV on a Supersonic Parachute Model," *47th Aerospace Sciences Meeting*, 2009. doi:10.2514/6.2009-70.

[2] Van Zante, D. E., and Wernet, M. P., "Tip Vortex and Wake Characteristics of a Counterrotating Open Rotor," *NASA/TM–2012-217713*, 2012.

[3] Bridges, J., and Wernet, M., "Measurements of the Aeroacoustic and Sound Source and in Hot Jets," *NASA/TM–2004-212508*, 2004.

[4] Bridges, J., and Wernet, M. P., "Establishing Consensus Turbulence Statistics for Hot Subsonic Jets," *16th AIAA/CEAS Aeroacoustics Conference*, 2010. doi:10.2514/6.2010-3751.

[5] Wernet, M. P., Georgiadis, N. J., Locke, R., Thurman, D., and Poinsatte, P., "PIV and Rotational Raman-Based Temperature Measurements for CFD Validation of a Perforated Plate Cooling Flow: Part I," *AIAA Scitech 2020 Forum*, American Institute of Aeronautics and Astronautics, 2020. doi:10.2514/6.2020-1230.

[6] Wernet, M. P., "Development of digital particle imaging velocimetry for use in turbomachinery," *Experiments in Fluids*, Vol. 28, No. 2, 2000, pp. 97–115. doi:10.1007/s003480050015.

[7] Chriss, R. M., Keith, T. G., Hingst, W. R., Strazisar, A. J., and Porro, A. R., "An LDA investigation of three-dimensional normal shock-boundary layer interactions in a corner," *19th AIAA, Fluid Dynamics, Plasma Dynamics, and Lasers Conference*, 1987. doi:10.2514/6.1987-1369.

[8] Soeder, R. H., Stark, D. E., Leone, J. F. X., and Henry, M. W., "NASA Glenn 1– by 1– Foot Supersonic Wind Tunnel User Manual," *NASA/TM–1999-2084789/Rev1*, 2003.

[9] Sobachkin, A., and Dumnov, G., "Numerical basis of CAD-embedded CFD," *NAFEMS World Congress*, 2013.

[10] Melling, A., "Tracer particles and seeding for particle image velocimetry," *Measurement Science and Technology*, Vol. 8, No. 12, 1997, pp. 1406–1416. doi:10.1088/0957-0233/8/12/005.

[11] Urban, W. D., and Mungal, M. G., "Planar velocity measurements in compressible mixing layers," *Journal of Fluid Mechanics*, Vol. 431, 2001, pp. 189–222. doi:10.1017/S0022112000003177.

[12] Ragni, D., Schrijer, F. F., Van Oudheusden, B. W., and Scarano, F., "Particle tracer response across shocks measured by PIV," *Experiments in Fluids*, Vol. 50, No. 1, 2011, pp. 53–64. doi:10.1007/s00348-010-0892-2.

[13] Mitchell, D., Honnery, D., and Soria, J., "Particle relaxation and its influence on the particle image velocimetry cross-correlation function," *Experiments in Fluids*, Vol. 51, No. 4, 2011, pp. 933–947. doi:10.1007/s00348-011-1116-0.

[14] Reising, H. H., and Davis, D. O., "Development and Assessment of a New Particle Image Velocimetry System in the NASA GRC 225 cm^2 Wind Tunnel," *AIAA SciTech 2023*, National Harbor, MD, 2023. doi:10.2514/6.2023-0631.

[15] Williams, O. J., Nguyen, T., Schreyer, A.-M., and Smits, A. J., "Particle response analysis for particle image velocimetry in supersonic flows," *Physics of Fluids*, Vol. 27, No. 7, 2015, p. 076101. doi:10.1063/1.4922865.

[16] Loth, E., "Compressibility and Rarefaction Effects on Drag of a Spherical Particle," *AIAA Journal*, Vol. 46, No. 9, 2008, pp. 2219–2228. doi:10.2514/1.28943.

[17] Peters, C. J., Pastor-Barsi, C. M., and Davis, D. O., "1- by 1-Foot Supersonic Wind Tunnel Sidewall Flowfield Compression Plate Study," *NASA/TM–20205008519/REV1*, in preparation, 2023.

[18] Laufer, J., "Aerodynamic Noise in Supersonic Wind Tunnels," *Journal of the Aerospace Sciences*, Vol. 28, No. 9, 1961, pp. 685–692. doi:10.2514/8.9150.